Chapter

4

Synthesis and characterization of surfactant/DES modified GO@TiO_2 NC for adsorption of dye from aqueous background

Contents

This chapter is mainly focused on covalent functionalization of GO@TiO_2 through surfactants and DES. The modified NCs is characterized using FTIR, XRD, FESEM-EDX and TGA. The dye adsorption study of the prepared NCs is also discussed in this chapter. The modified NCs is a suitable material for waste water treatment.

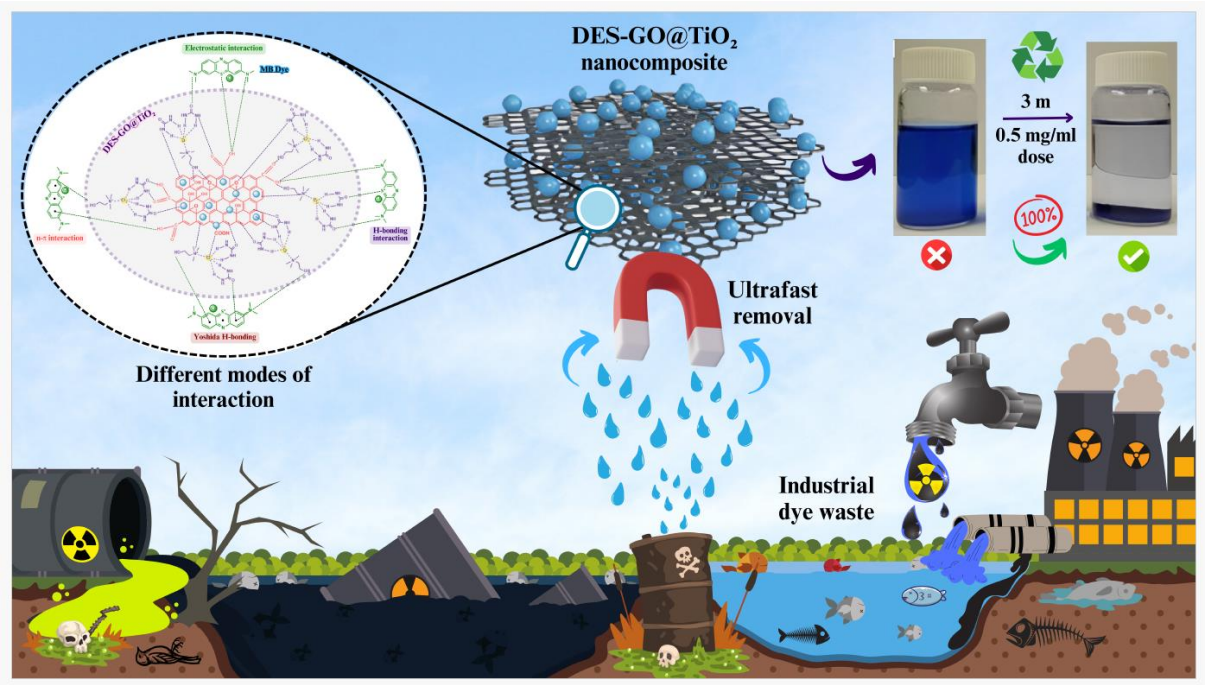

4.1 Introduction

Extensive industrialization and urban development are the main factors behind wastewater discharge, leading to significant water pollution. One significant issue is the release of dyes into water bodies, posing threats to terrestrial/aquatic life alike. The disposal of effluents containing used dyes into water bodies is a significant contributor to water pollution. Treatment is crucial to mitigate the harmful impacts of discharged dyes in wastewater before disposal. However, dye removal remains a challenging problem, as even a small amount can lead to health issues such as allergic reactions, skin irritation, and cancer. Various techniques, including physical, photocatalysis, electrochemical, chemical, adsorption, and biological treatment, have been employed to address this issue. Among these, adsorption stands out as the most effective method due to its simplicity, cost-effectiveness, and versatility in selecting and modifying adsorbent material. Moreover, it generates no harmful by-products and can be applied effectively to treat large volumes of water [1]. Various analytical instruments, including GC–MS [2], LC-MS [3], and HPLC-DAD [4], have been

established for dye detection. While these hyphenated techniques offer rapid and precise results [5], they pose drawbacks like high costs, complex instrumentation, and the use of organic reagents. Therefore, sustainability demands a method that delivers fast, accurate, and cost-effective analysis. UV-visible spectroscopy stands out as an alternative detection technique that is user-friendly, provides quick and accurate results, and imparts economy to the entire process [6].

As established in earlier discussions, GO is chosen over pure graphene for its functional groups and exceptional properties. Challenges include surface energy-induced agglomeration and higher costs. These are addressed by incorporating metallic oxides through NC formation [7–9]. Among the metal oxides employed in the formation of composite, titanium (IV) oxide (TiO_2) has drawn special attention from the research community. This is due to its easy availability, long-term stability, cost-effectiveness, non-toxic nature, biocompatibility, environmental friendliness, and high chemical stability [10–13], making it a promising precursor of nanomaterial for large-scale industrial wastewater treatment [14]. NCs are currently being modified/functionalized with a range of compounds/mixtures, like polymers (synthetic/natural), surfactants, or ionic liquids among others [15–20].

Surfactants are preferred as modification agents as discussed in previous chapters [21–25]. Among various charge types, cationic surfactants have demonstrated superiority as modifiers, outperforming other classes of materials [22,26,27]. Cationic surfactants effectively adsorb onto the carboxyl groups of GO through electrostatic attraction, leading to the formation of insoluble complex salts [28,29]. The use of cationic surfactant-modified NCs based on metal oxides and GO has been documented in several scholarly publications [19,30].

As previously discussed, DESs have diverse applications in nanomaterial synthesis, processing, and functionalization [31–33]. Their adaptability allows for the efficient exfoliation of 2D nanosheets and the functionalization of carbon-metallic nanomaterials [34–38]. Notably, while surface-functionalized pre-synthesized graphene-iron nanohybrids using DESs have been explored for analytical purposes [39] , there is a gap in studies examining the potential of DESs as coupling agents for linking GO and TiO_2. Therefore, it is essential to compare the roles of DES and surfactants as modifiers. In this context, the challenge of eliminating MB, a synthetic dye extensively used in various industries [40], remains a formidable task for present-day researchers.

In this chapter, our primary objective was to utilize DES and cationic surfactant to facilitate the coupling of GO nanosheets with TiO_2 nanoparticles. Our objective was to experimentally verify the theory that the amine functionalization of GO surfaces using *reline* as a DES would allow us to attach TiO_2 nanoparticles without the need for initial functionalization of TiO_2. The basis of

the hypothesis lies in the intrinsic affinity of TiO_2 nanoparticles for amine functional groups, and the surfactant/DES functionalized GO surfaces can provide such a situation [14]. Furthermore, GO functionalized with DES would offer favourable chemistry for H-bond formation between GO and TiO_2 (DES-GO@TiO_2). Our secondary objective involved the intercalation of GO-TiO_2 with DTAB through non-covalent interactions (DT-GO@TiO_2) [19,41]. To compare adsorption and its kinetics, MB has been taken as a model dye. DTAB and *reline* are well-known cationic surfactant and DES, respectively. In the present study, modified NCs through various physicochemical methods. Various experimental conditions were optimized to maximize dye removal from the aqueous medium. To address the economic part of the procedure, the adsorbent has been used for a number of repeat cycles, and their performances are scrutinized. The rate of MB content adsorbed per gram of adsorbent per second has also been computed to single out the best material among similar classes. The strategies presented here hold the potential to contribute to the mitigation of water pollution and the overall environmental cleanup efforts.

4.2 Experimental section

The materials and methods used are discussed in chapter 2.

4.3 Results and Discussion

4.3.1 XRD

XRD spectra of TiO_2, GO@TiO_2, DT-GO@TiO_2, and DES-GO@TiO_2 NCs are shown in **Figure 4.1**. The characteristic peaks were found at 20.8°, 25.82°, 28.79°, 30.84°, 36.05°, 41.07°, 50.92°, and 54.27° corresponds to crystal plane (101), (004), (200), (105), (211), (204), (116) and (002) for the TiO_2 nanoparticle sample [42]. In the XRD pattern of GO/TiO_2 NC, all diffraction peaks are similar to TiO_2 nanoparticles [43,44]. However, the main diffraction peak of GO has disappeared due to the coating TiO_2 on it. The intensity of the peak's characteristic of the TiO_2 anatase phase in the DT-GO@TiO_2 and DES-GO@TiO_2 NC was significantly reduced compared to that of pure TiO_2 nanoparticles. This reduction suggests that the TiO_2 nanoparticles were well coated between the GO sheets. Furthermore, the characteristic peaks of the TiO_2 phase in the DT-GO@TiO_2 and DES-GO@TiO_2 NC shifted to smaller angles. This shift is attributed to the formation of metal oxides on the GO surfaces. Additionally, no characteristic peaks of GO, DES, and DTAB were observed in the NCs, indicating the successful integration of TiO_2 nanoparticles onto the GO surfaces.

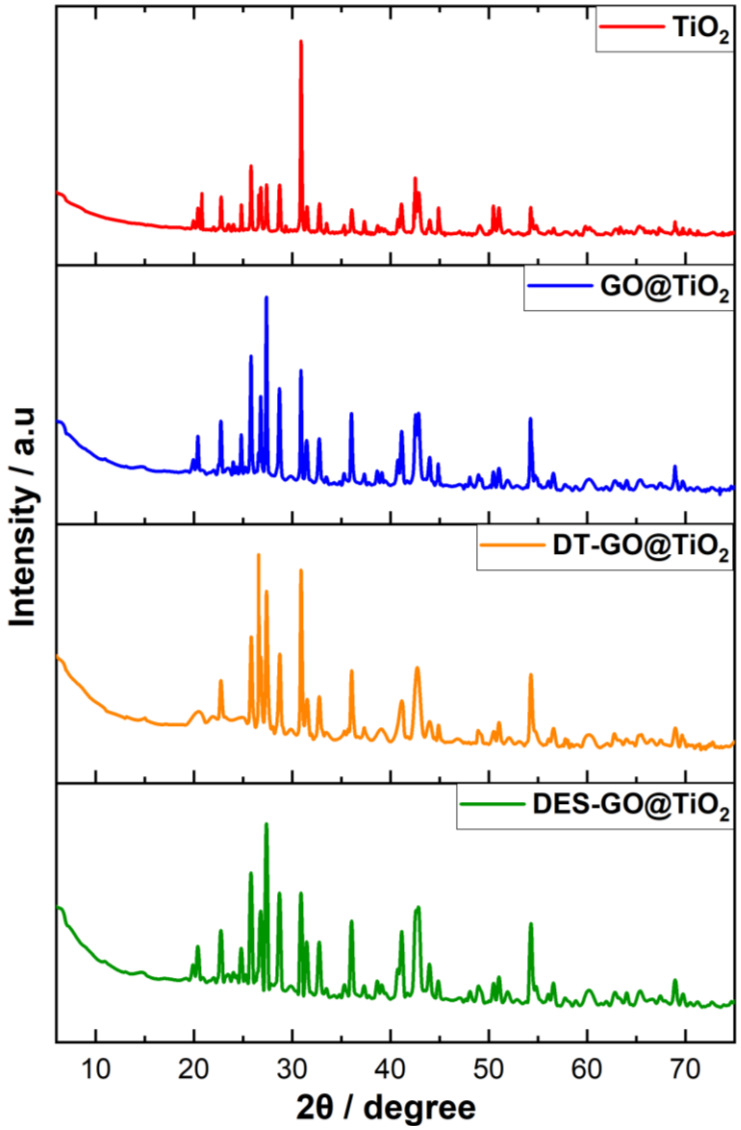

Figure 4.1: XRD spectra of TiO_2, GO@TiO_2, DT-GO@TiO_2 and DES-GO@TiO_2 NCs.

4.3.2 FTIR

FT-IR spectra for GO@TiO_2, DT-GO@TiO_2, and DES-GO@TiO_2 are shown in **Figure 4.2**. The band observed at 3256 cm^{-1} in all spectra can be attributed to O-H stretching vibrations, which are a result of the presence of hydroxyl groups [45]. The spectra also indicated the presence of various other chemical groups, such as C=O (1708 cm^{-1}), C–O–C (1075 cm^{-1}, 1082 cm^{-1}, and 1086 cm^{-1}), C=C (1567 cm^{-1}), and C–OH (1530 cm^{-1}) [43,44]. The absorption peak observed at 603 cm^{-1} is assigned to the stretching vibration of Ti-O-Ti, and it is noteworthy that the Ti-O-Ti absorption peak is reduced in the modified NCs. This observation suggests the possible existence of interaction between GO and TiO_2. 1561 cm^{-1} and 1082 cm^{-1} peaks are sharpened in the case of

modified NCs because of C=C and C-O stretching, respectively. The data suggests the successful functionalization of the GO@TiO_2 NC by coupling through DES and DTAB.

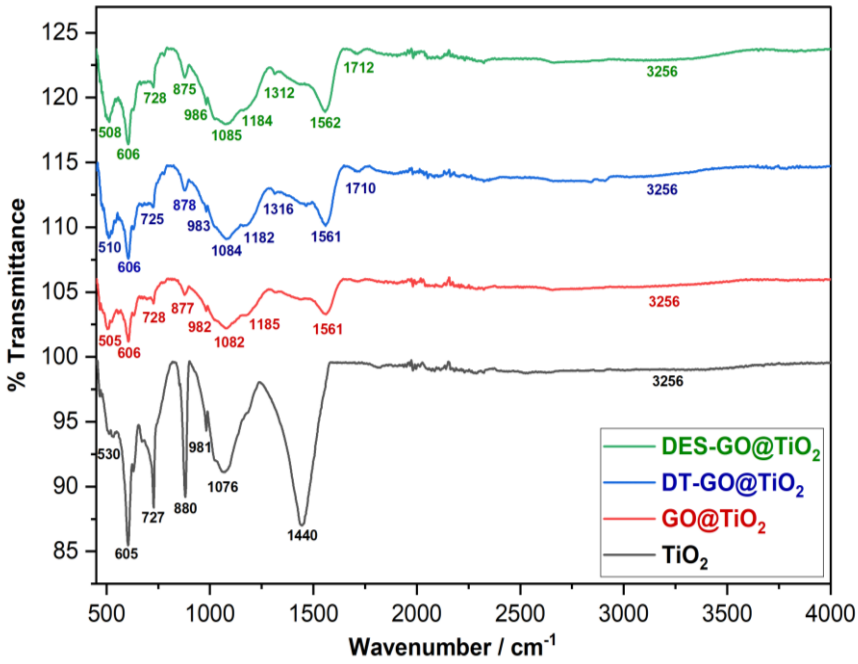

Figure 4.2: FTIR spectra of TiO_2, GO@TiO_2, DT-GO@TiO_2 and DES-GO@TiO_2 NCs.

4.3.3 FESEM-EDX

FESEM-EDX data is presented in **Figure 4.3 (I to III)** to provide additional confirmation of the modification of the GO@TiO_2 NC. The EDX elemental maps show the presence of carbon (C), oxygen (O), nitrogen (N), titanium (Ti), bromine (Br), and chlorine (Cl) in the modified NCs. This demonstrates the effective bonding of GO nanosheets and TiO_2 nanoparticles through surface modification with DES and DTAB. Furthermore, the elemental maps validated the uniform dispersion of TiO_2 nanoparticles on the graphene nanosheets. The FESEM image of DES/GO-TiO_2 NC reveals a higher degree of aggregation in the graphene structures, with TiO_2 nanoparticles uniformly distributed all over and covering a substantial portion of the surface. Upon enlarging the FESEM image of DT-GO@TiO_2 NC, certain wrinkles become apparent in these sheets. These wrinkles are likely a consequence of the repulsive negative charges from the deprotonated carboxylic acid groups present on the GO sheets [19]. The lamellar structure contributes to a substantial surface area in the composite, and this feature is vital for its potential applications in the adsorption of dye molecules. The EDX spectra with mapping show the presence of C, N, O, and Ti atoms for GO@TiO_2 NC (**Figure 4.3 (I)**), the presence of C, N, O, Ti and Br atoms for DT-GO@TiO_2 NC (**Figure 4.3 (II)**), and the presence of C, N, O, Ti and Cl atoms for DES-GO@TiO_2 NC (**Figure 4.3 (III)**) indicating the successful functionalization of NCs.

(I)

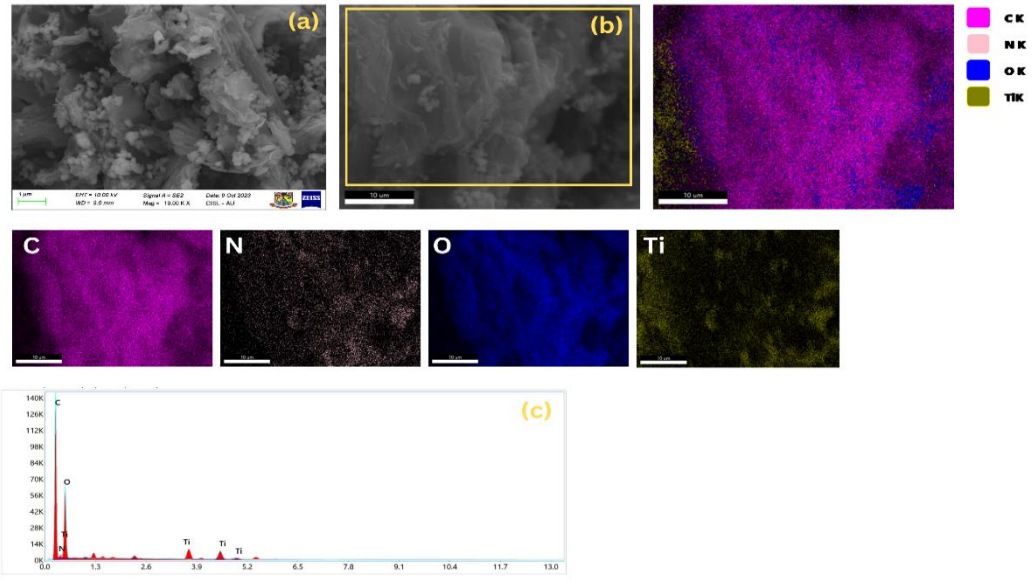
(a)
(b)
CK
NK
OK
TiK
C
N
O
Ti
(c)
C
O
Ti
Ti
Ti

(II)

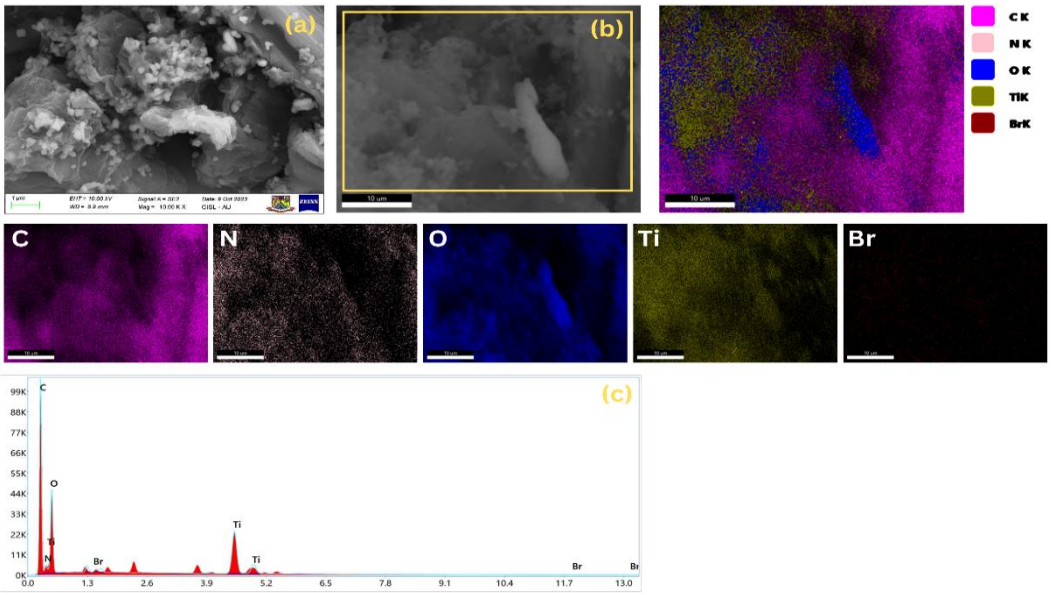
(a)
(b)
CK
NK
OK
TiK
BrK
C
N
O
Ti
Br
(c)
C
O
Ti
Ti
Br
Br
Br

(III)

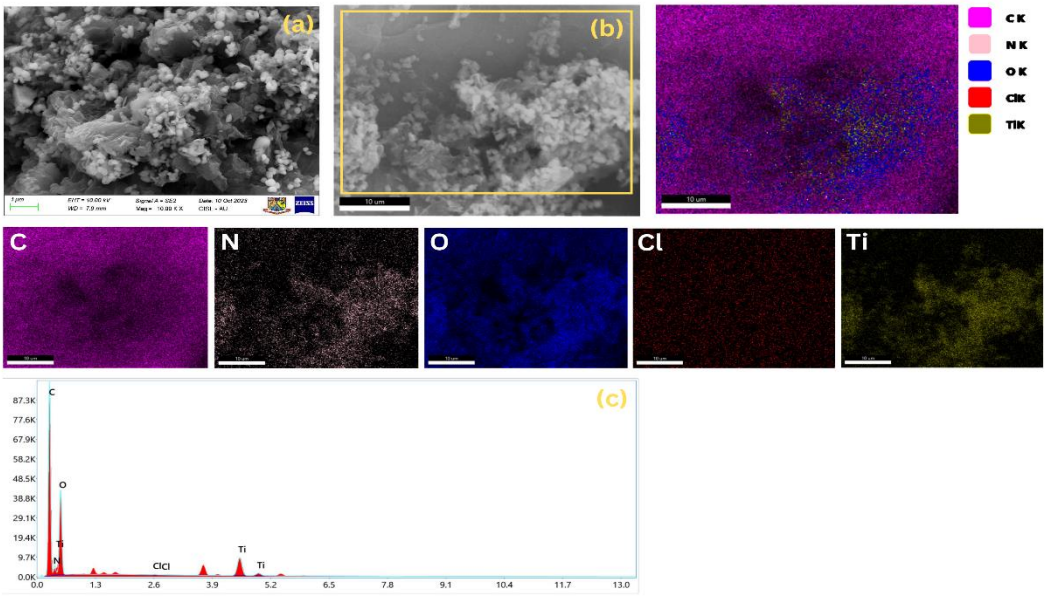
(a)
(b)
CK
NK
OK
ClK
TiK
C
N
O
Cl
Ti
(c)
C
O
Ti
Ti
ClCl

Figure 4.3: FESEM/EDX analysis of (I) GO@TiO_2, (II) DT-GO@TiO_2 and (III) DES-GO@TiO_2 NC's (a) FESEM image, (b) EDX elemental mapping showing different elements, (c) spot EDX spectra showing various elements in terms of percentage.

4.3.4 TGA

Figure 4.4 (I) and (II) display TGA thermograms and derivative thermograms for both the pure and modified NCs. GO@TiO_2 displays enhanced thermal stability, attributed to the strong interaction between TiO_2 and GO sheets [46,47]. The DES-GO@TiO_2 NC exhibited weight loss within the temperature range of 300-550 °C, likely attributed to the decomposition of nitrogen and chloride groups found on the surface. Moreover, the increased weight loss observed in DT-GO@TiO_2 NC is due to the decomposition of quaternary ammonium moieties. Following the decomposition of thermally sensitive oxygen functionalities and other functional groups, there was no significant mass loss observed up to 700 °C (**Figure 4.4**).

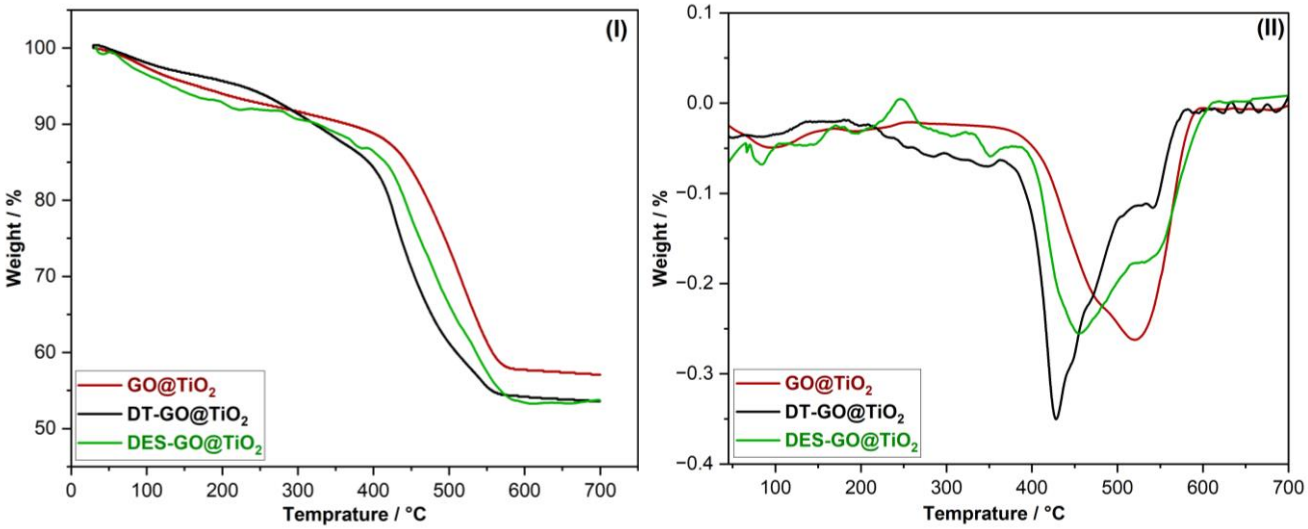

Figure 4.4: (I) TGA (II) derivative thermograms of GO@TiO_2, DT-GO@TiO_2 and DES-GO@TiO_2 NCs.

4.3.5 Effect of [MB]

The adsorption process was utilized to investigate the removal of MB from an aqueous dye solution under static conditions. A consistent composite dose (0.5 mg/mL for each GO@TiO_2, DT-GO@TiO_2, and DES-GO@TiO_2) was present during the experiments. The percentage of MB removal (P) was plotted against various fixed concentrations of MB (20-100 mg L^{-1}) for all conditions after a duration of 60 m, followed by centrifugation. The results are illustrated in **Figure 4.5**. An examination of the data from **Figure 4.5** indicates that the modification enhances the P value match to what was observed with GO@TiO_2. The P value decreased as the [MB] increased. With the increase in [MB], the available adsorption sites became limited, resulting

in a decrease in dye removal before reaching equilibrium. In this experimental setup, the optimal performance in terms of MB adsorption was observed at a concentration of 20 mg L^{-1} for DES-GO@TiO_2 and DT-GO@TiO_2. Hence, these concentrations were selected for optimizing the composite dosages.

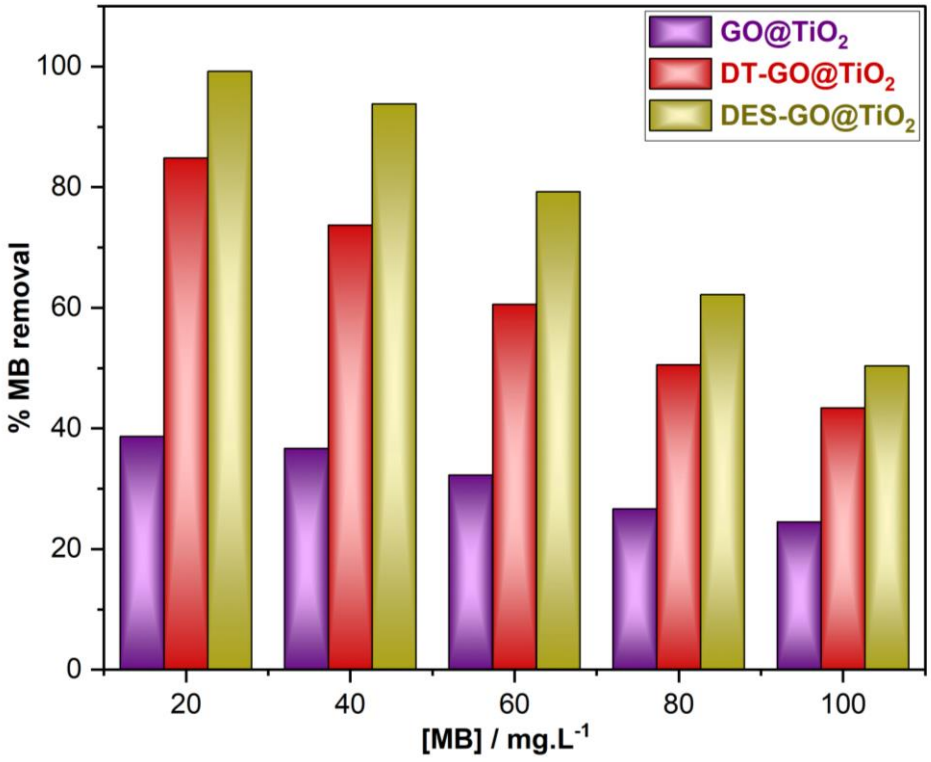

Figure 4.5: The effect of the initial dye concertation on the percentage removal of MB for GO@TiO_2, DT-GO@TiO_2 and DES-GO@TiO_2 NCs.

4.3.6 Effect of Composite Load

Fixed concentrations of MB were employed to examine how the composite loading affects the absorption capacity of MB from an aqueous solution. The load of NC was varied from 3-40 mg (0.15 to 2 mg/mL) to establish the optimal adsorbent content for MB removal (after 60 m). Data for DES-GO@TiO_2 and DT-GO@TiO_2 are depicted in **Figure 4.6**. The results show a swift increase in the efficiency of dye removal, i.e., from 83.4 to 99.9%, as the amount of the DES-GO@TiO_2 increases from 5 to 10 mg, which then becomes constant. Similarly, rapid increase in the efficiency of dye removal, i.e., from 85.75 to 99.9%, as the amount of the DT-GO@TiO_2 increases from 10 to 20 mg, which then becomes constant. Subsequent increments in the composite load did not impact the efficiency of dye removal, as the maximum amount of dye had

already been adsorbed, and no additional dye molecules were available for adsorption. Therefore, a 10 mg (0.5 mg/mL) composite load was taken to optimize for the pH effect.

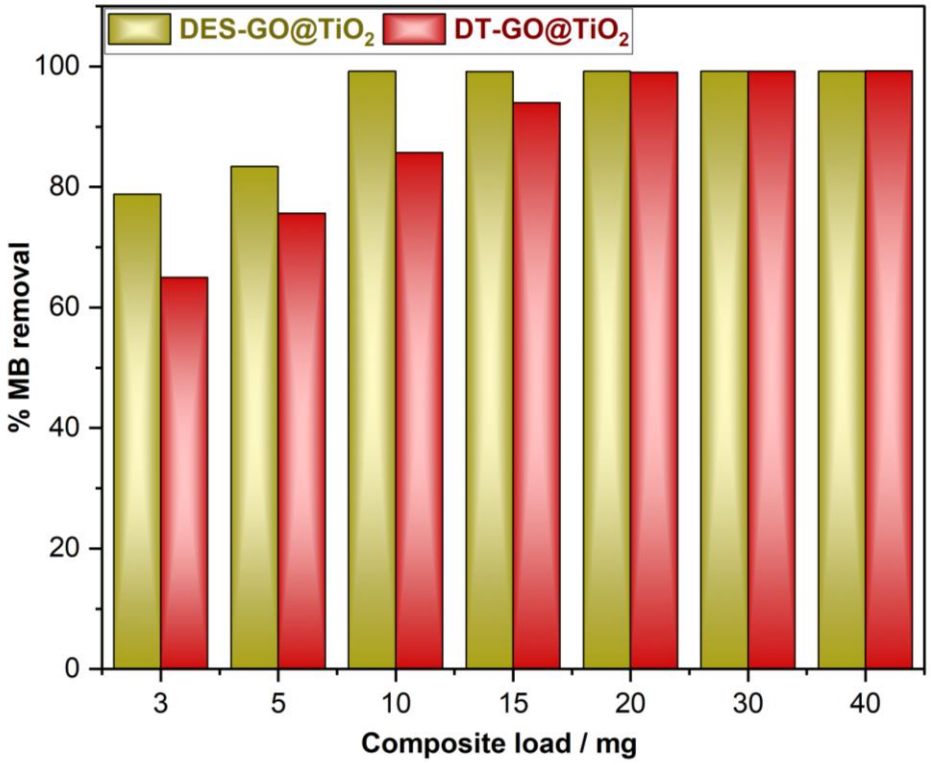

Figure 4.6: The effect of the composite load on the percentage removal of MB for DT-GO@TiO_2 and DES-GO@TiO_2 NCs.

4.3.7 Effect of pH

The initial pH of the dye solution is considered crucial as it often affects dye adsorption. The pH adjustments were achieved by adjusting the concentrations of NaOH or HCl, depending on the targeted pH range (basic/acidic). As the pH increases, MB molecules will be present in either charged or uncharged forms. The changes in P vs. pH for the systems introduced in section 2.6 (after 60 m) are depicted in **Figure 4.7.** It was observed that for DES-GO@TiO_2 the P increased rapidly from pH 2 (64.70%) to pH 7 (78.4%) and reached the highest P value at pH 10 (~99%). Similarly, for DT-GO@TiO_2 the P increased from pH 2 (57.35%) to pH 7 (69.4%) and reached the highest P value at pH 10 (~95%). The MB adsorption is increased with an increase in pH for both NCs, attributed to the surface charge of the composite adsorbent and the charge of MB. **Figure 4.8** illustrates the variation of ΔpH vs. $pH_{initial}$, revealing a pH_{pzc} close to zero within the pH range of 7 to 8. Above this pH range, the surface of the NC will carry a negative charge, which promotes the attraction of the cationic form of the dye. This leads to a significant rise in the P value from pH 8 to 10. This observation aligns with the pKa value of MB, which is 3.8 [48]. The increase in the P value with pH is consistent with a previous study that investigated MB

adsorption on a GO-based composite [49]. When the pH exceeds the pKa, MB dye molecules are present in their cationic form [50]. Therefore, raising the pH of the dye solutions led to an augmentation in the electrostatic attraction between the positively charged MB molecules and the negatively charged NCs surface. Therefore, a pH of 10 was selected as the optimal condition for further MB adsorption studies.

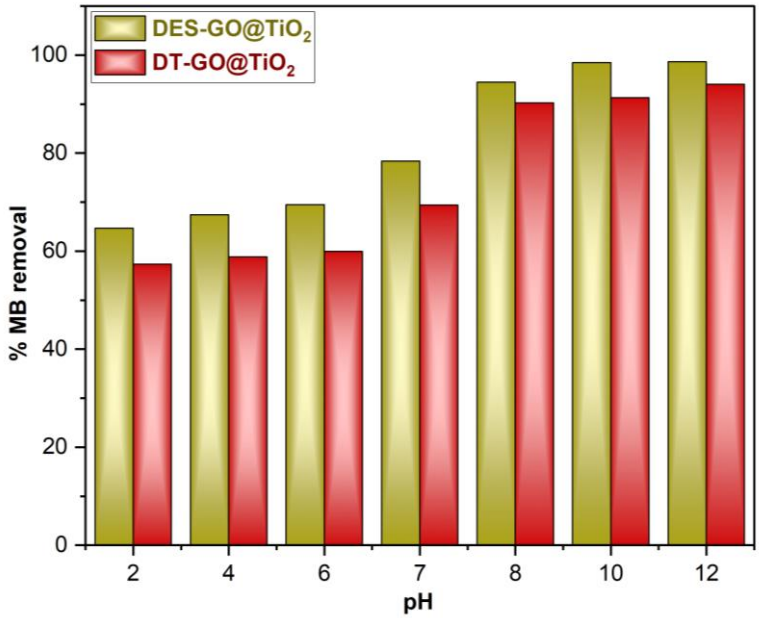

Figure 4.7: The effect of the pH on the percentage removal of MB for DT-GO@TiO_2 and DES-GO@TiO_2 NCs.

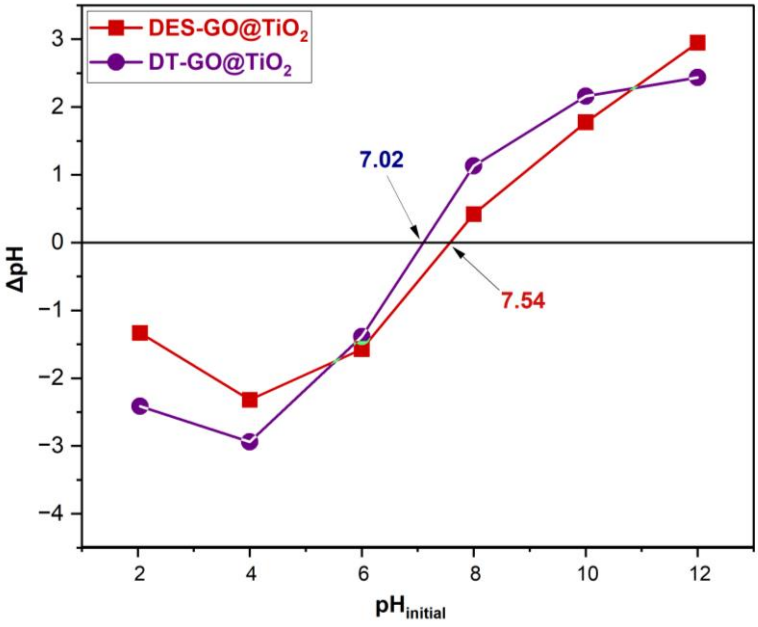

Figure 4.8: Point of zero charge (pH_{pzc}) of DT-GO@TiO_2 and DES-GO@TiO_2 NCs.

4.3.8 Effect of Contact Time: Adsorption Kinetics

To comprehend the kinetics of the adsorption process, the effects of contact time and the [MB] were examined while keeping the composite concentration fixed at 0.15-2 mg/mL and the pH at 10. The adsorption data at various time intervals (Q_t) were graphed against time (t), and these profiles are depicted in **Figure 4.9 (I & II)**. This data was utilized for determining Q_e, representing the quantity of MB adsorbed per gram of composite upon reaching equilibrium. To analyze adsorption kinetics, diverse kinetic models (*pseudo*-first order, *pseudo*-second order, and intraparticle diffusion models) were applied. The Lagergren equation, a commonly adopted model for both liquid and solid systems, was employed to assess *pseudo*-first order kinetics [51].

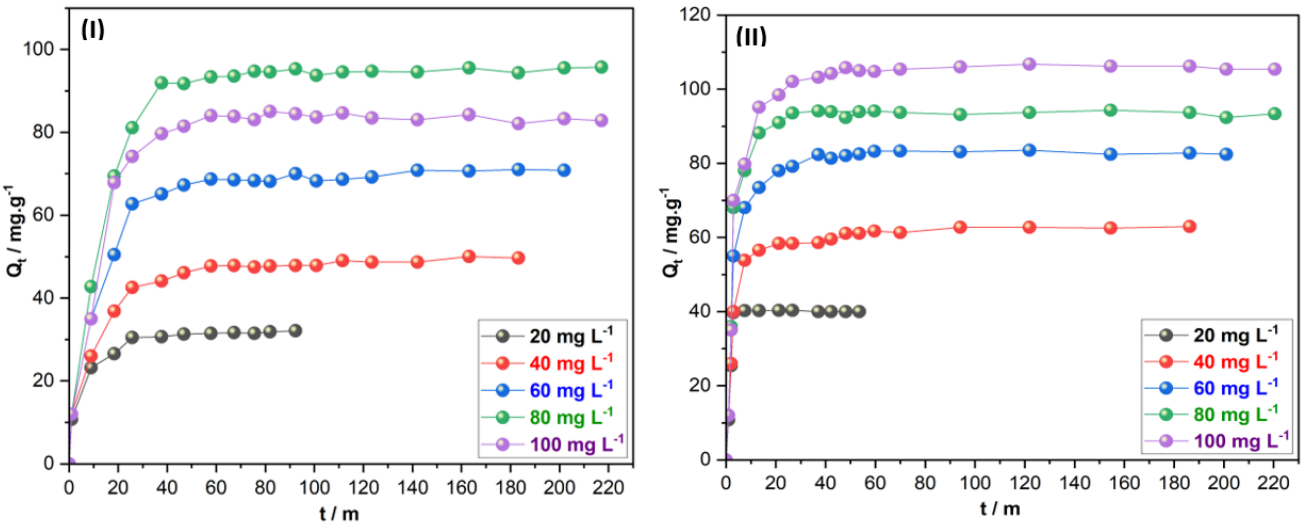

Figure 4.9: Variation of adsorption capacity (Q) with time (t, m) for MB dye on (I) DT-GO@TiO_2 and (II) DES-GO@TiO_2 NCs.

4.3.8.1 Pseudo-first order kinetic model

$$\ln(Q_e - Q_t) = \ln Q_e - k_1 t \qquad (4)$$

In this equation, k_1 (min^{-1}) denotes the rate constant for the *pseudo*-first order kinetics of MB adsorption. The values of Q_e and k_1 can be ascertained from the slope and intercept of log (Q_e - Q_t) vs. t plots (as shown in **Figure 4.10 (a & b)**). The calculated data relevant to this model can be found in **Table 4.1**. An examination of **Figure 4.10** clearly indicates that the kinetic data cannot be fitted to the current model (for both NCs, as shown in **Figure 4.10 (a & b), Table 4.1**). Hence, alternative models have been examined. The square of the correlation coefficient (R^2) values for different MB concentrations is consistently below one, suggesting that the *pseudo*-first

order kinetic model is not appropriate. This is further substantiated by substantial disparities between the experimentally observed Q_e and the theoretically calculated Q_e (**Table 4.1**).

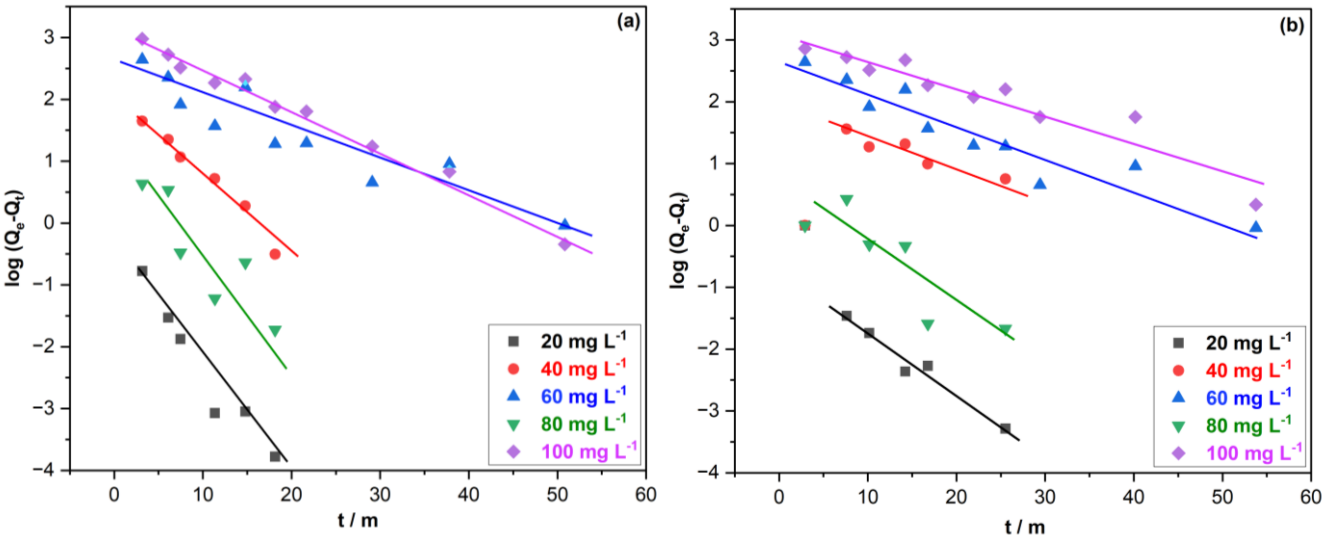

Figure 4.10: Variation of log (Q_e-Q_t) vs. *t* and fitted data of *pseudo*-first order kinetic model: a) DT-GO@TiO_2, and b) DES-GO@TiO_2 at 30°C.

Table 4.1: Fitted kinetic data in different models for DES-GO@TiO_2 and DT-GO@TiO_2

DES-GO@TiO_2										
Adsorbent (mg/L)	Pseudo-first order				Pseudo-second order			Intra-particle diffusion		
	$Q_e(exp)$ (mg g^{-1})	$Q_e(cal)$ (mg g^{-1})	k_1 (min^{-1})	R^2	$Q_e(cal)$ (mg g^{-1})	k_2 (g $mg^{-1}min^{-1}$)	R^2	k_i	C_i	R^2
20	39.68	25.65	0.0835	0.856	35.44	0.3572	0.998	1.956	2.658	0.964
40	75.06	50.49	0.0841	0.326	69.35	0.1475	0.999	2.654	5.964	0.976
60	95.1	80.21	0.0772	0.489	91.34	0.0228	0.999	2.341	6.219	0.856
80	99.48	85.94	0.0778	0.374	95.67	0.0036	0.998	2.333	3.452	0.921
100	100.74	95.47	0.0575	0.659	98.66	0.0025	0.997	2.981	8.277	0.946
DT-GO@TiO_2										
Adsorbent (mg/L)	Pseudo-first order				Pseudo-second order			Intra-particle diffusion		
	$Q_e(exp)$ (mg g^{-1})	$Q_e(cal)$ (mg g^{-1})	k_1 (min^{-1})	R^2	$Q_e(cal)$ (mg g^{-1})	k_2 (g $mg^{-1}min^{-1}$)	R^2	k_i	C_i	R^2
20	37.61	22.36	0.0689	0.885	30.64	0.2494	0.999	2.659	6.512	0.958
40	69.54	45.86	0.0981	0.239	51.29	0.0865	0.997	2.551	5.882	0.913
60	72.70	62.37	0.0845	0.113	53.24	0.0516	0.995	3.264	6.641	0.862
80	80.94	69.55	0.0653	0.387	65.98	0.0021	0.999	1.189	4.437	0.756
100	86.86	72.41	0.0642	0.209	68.79	0.0013	0.998	1.112	3.219	0.877

4.3.8.2 Pseudo-second order kinetic model

The *pseudo*-second-order kinetic equation has been determined using the data for MB adsorption with both NCs in order to validate the kinetic model [52]

$$\frac{t}{Q_t} = \frac{1}{k_2 Q_e^2} + \frac{t}{Q_e} \quad (5)$$

The rate constant for the second order reaction, denoted as k_2 (g mg^{-1} min^{-1}), and Q_e was derived from the slope and intercept of the linear plot of t/Q_t vs. t, as illustrated in **Figure 4.11 (a & b)**. It's important to remember that the adsorption rate and initial adsorption speed are equal when t→0. **Table 4.1** provides a summary of the model's data. The *pseudo*-second order kinetic model appears to be a good fit for interpreting the MB adsorption kinetics on either modified NCs (DT-GO@TiO_2 and DES-GO@TiO_2), based on the increased R^2 values (~1).

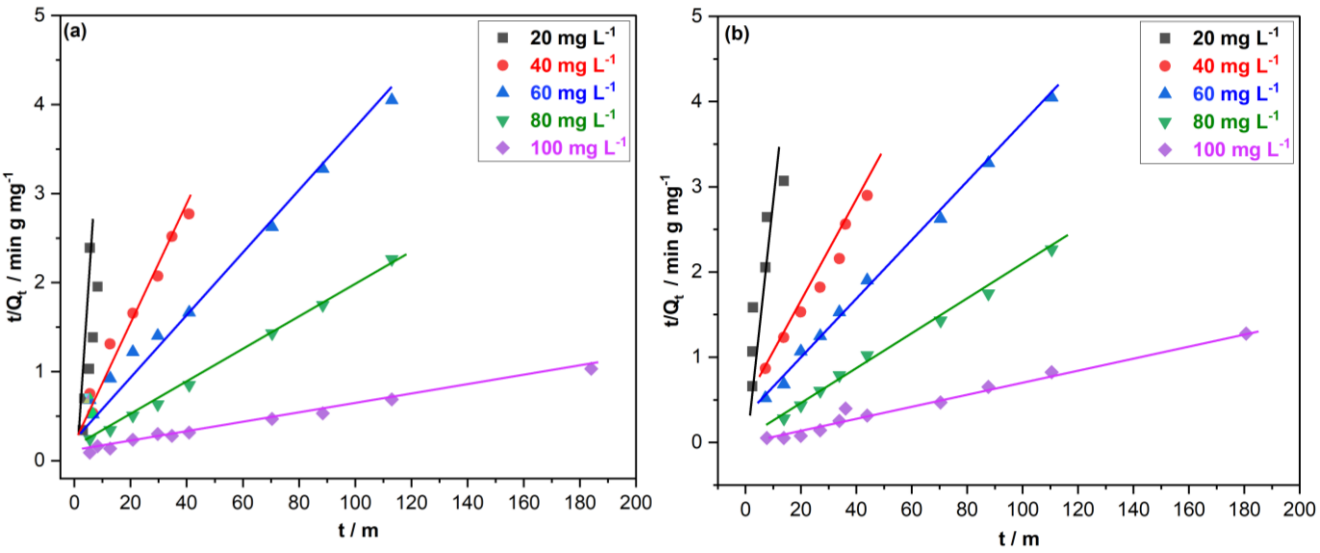

Figure 4.11: Variation of t/Q_t vs. t and fitted data of *pseudo*-second order kinetic model: a) DT-GO@TiO_2, and b) DES-GO@TiO_2 at 30°C.

4.3.8.3 Intraparticle diffusion kinetic model

Another kinetic model that considers both the diffusion process of the adsorbate and concentration variation has been used to interpret the adsorption behaviour. The expression for this model is as follows [53],

$$Q_t = k_i t^{1/2} + C_i \quad (6)$$

k_i is the intraparticle velocity constant (mg g^{-1} $min^{1/2}$), and C_i is a constant related to the boundary layer thickness/diffusion. If the plot of Q_t vs. $t^{½}$ results in a linear relationship (**Figure 4.12 (a & b)**), the slope and intercept can be employed to determine the values of k_i and C_i. **Table 4.1** displays the computed values of k_i, C_i, and R^2. By examining the fitted data and R^2 values (which are much less than 1), it is possible to conclude that mechanisms other than pore/surface diffusion are also in effect. One such mechanism may be film diffusion.

Upon reviewing all the fitted data with various kinetic models for both NCs (as presented in **Table 4.1**), it becomes evident that the better fitting (**Figure 4.11 (a & b)**) and acceptable R^2 values are achieved with the *pseudo*-second order kinetic model. This means that the best possible model to explain MB's adsorption on the surfaces of both modified NCs is probably the *pseudo*-second order model.

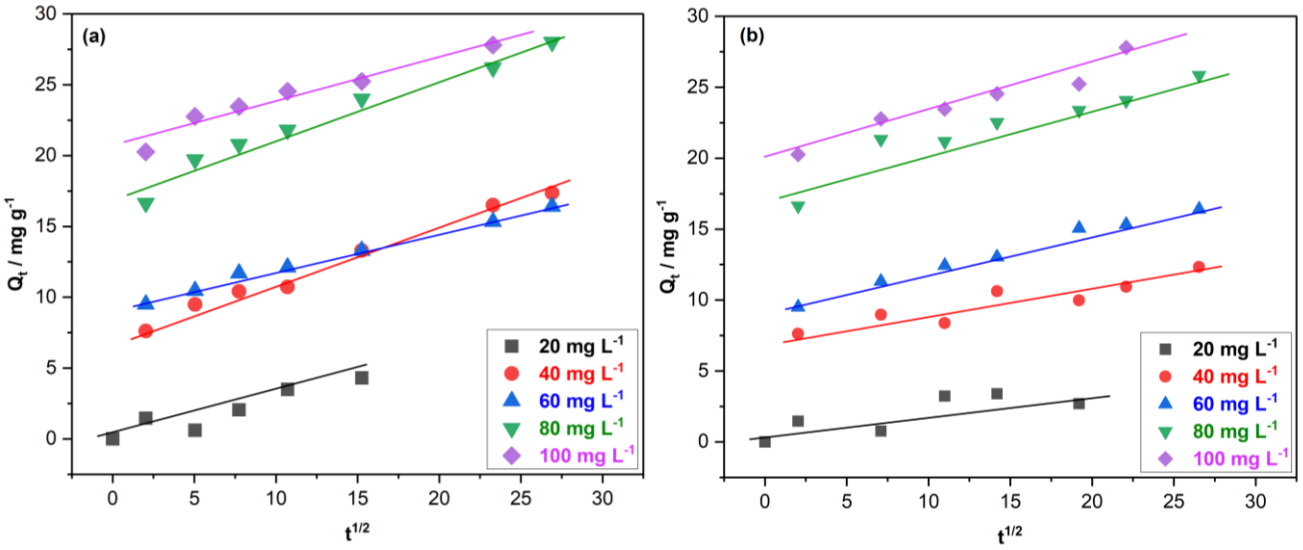

Figure 4.12: Variation of Q_t vs. $t^{1/2}$ and fitted data of Intraparticle diffusion kinetic model: a) DT-GO@TiO_2, and b) DES-GO@TiO_2 at 30°C.

4.3.9 Adsorption isotherm

This study has assessed the efficacy of several adsorption isotherm models (at 30 °C), including the Freundlich, Langmuir, and Temkin models.

4.3.9.1 Freundlich isotherm

According to the Freundlich adsorption model, the surface of the composite is heterogeneous and capable of supporting multilayered adsorption. The following is a representation of the Freundlich isotherm model,

$$logQ_e = logK_{FI} + \frac{1}{n}\log C_e \qquad (7)$$

In the formula, n denotes the adsorption potency and K_{FI} (mg/g) is the Freundlich adsorption constant. The parameter n determines the spontaneity and reversibility of the process, with $0 < 1/n < 1$ indicating spontaneity, $1/n > 1$ indicating non-spontaneity, and $1/n = 1$ indicating non-reversibility. Analyzing the intercept and slope of the log Q_e vs. log C_e plots will yield the values of n and K_{FI} (**Figure 4.13**), where C_e represents the equilibrium concentration of

MB. The data given in **Table 4.2**, along with the low R^2 values, suggest that the Freundlich adsorption model is not applicable to express the adsorption of MB on the modified NCs. This implies that multilayer adsorption is not occurring in this system.

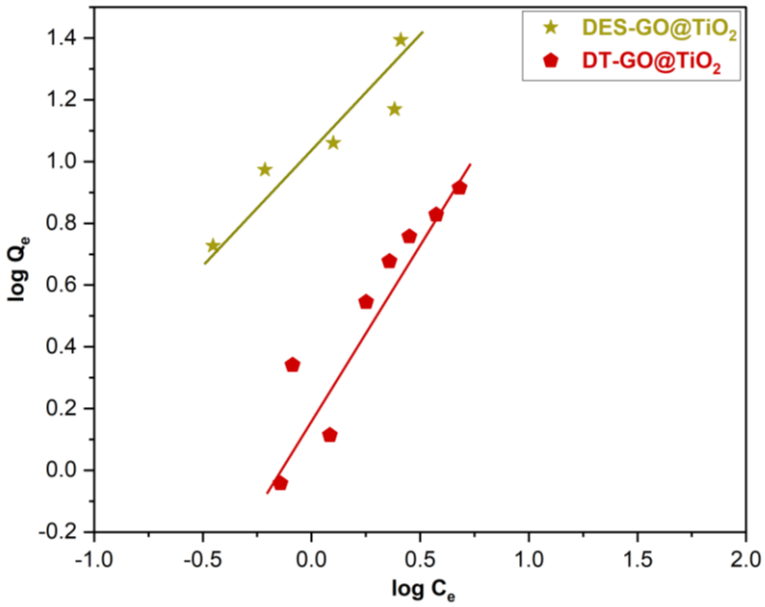

Figure 4.13: Variation of log Q_e vs. log C_e and fitted Freundlich isotherm model for DT-GO@TiO_2, and DES-GO@TiO_2 at 30°C.

Table 4.2: Fitted adsorption data of MB on DES-GO@TiO_2 and DT-GO@TiO_2 using various models.

Isotherms	Parameters	DES-GO@TiO_2	DT-GO@TiO_2
Freundlich	K_{FI} (mg/g)	15.64	11.98
	n	0.329	0.684
	R^2	0.846	0.912
Langmuir	Q_m (mg/g)	110.64	97.64
	b (L/mg)	2.864	3.251
	R^2	0.998	0.996
Temkin	K_T (L/g)	53.58	23.69
	2.303 RT/b	0.864	0.947
	R^2	0.784	0.885

4.3.9.2 Langmuir isotherm

Given that the Freundlich adsorption model does not adequately describe MB adsorption, the Langmuir isotherm model was used to elucidate the precise mechanism of MB adsorption. The Langmuir isotherm [54] is represented as follows:

$$\frac{1}{Q_e} = \frac{1}{Q_m} \times \frac{1}{b} \times \frac{1}{C_e} + \frac{1}{Q_m} \quad (8)$$

Q_m represents the amount of MB required to create a monolayer (mg/g), and b is a constant (L/mg) that signifies the energy of adsorption. Plotting $1/Q_e$ vs.$1/C_e$ yields a straight line with an intercept of $1/Q_m$ and a slope of 1/b. Q_m (**Figure 4.14**). The model's other adsorption constants are shown in **Table 4.2** along with the R^2 values, which were determined to be quite adequate. These findings imply that the Langmuir model can accurately represent the adsorption of MB onto modified NCs.

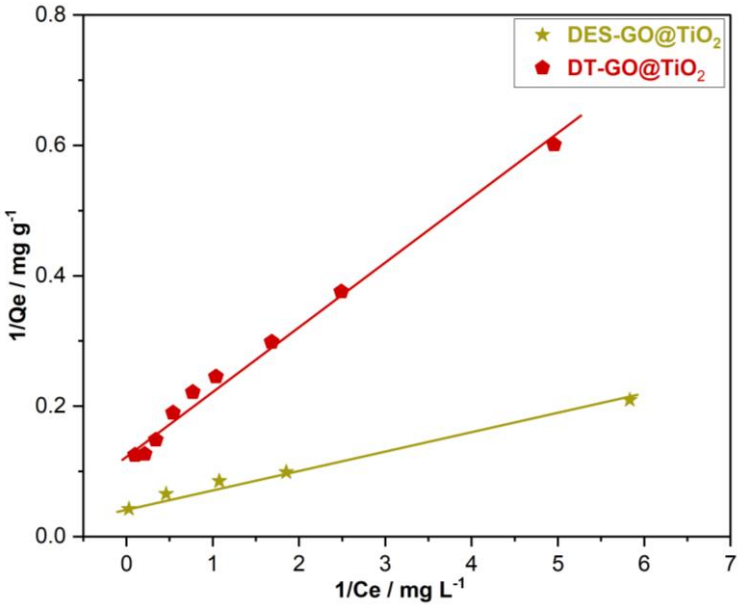

Figure 4.14: Variation of $1/Q_e$ vs. $1/C_e$ and fitted Langmuir isotherm model for DT-GO@TiO_2, and DES-GO@TiO_2 at 30°C.

4.3.9.3 Temkin isotherm

The Temkin isotherm was one additional well-known model to which the adsorption data were examined in order to confirm the validity of the Langmuir model [55]. According to this model, when the adsorbate reaches the adsorbent surface, the heat of adsorption linearly decreases. The mathematical representation of this model is as follows,

$$Q_e = 2.303 \frac{RT}{b} (\log K_T + \log C_e) \quad (10)$$

The term K_T (L/g) represents the Temkin constant, which is associated with the energy required for the MB binding to the modified NC. The value of RT/b, obtained from the slope and intercept of the Q_e vs. log C_e plot (**Figure 4.15**), provides insights into the nature of the adsorption process. If RT/b>0, the operation can be characterized as exothermic; conversely, if RT/b<0, it indicates an endothermic process where heat is absorbed during adsorption. **Table 4.2** lists the values of RT/b, K_T, and R^2 in detail.

Reviewing the isotherm parameters presented in **Table 4.2**, it is evident that the Langmuir model, representing monolayer adsorption, provides the best fit for the MB adsorption data when utilizing DT-GO@TiO_2 and DES-GO@TiO_2 as adsorbents. This suggests that monolayer adsorption of MB is occurring, accompanied by heat release. Consequently, it can be inferred that the binding affinity of MB to DES-GO@TiO_2 is stronger compared to DT-GO@TiO_2.

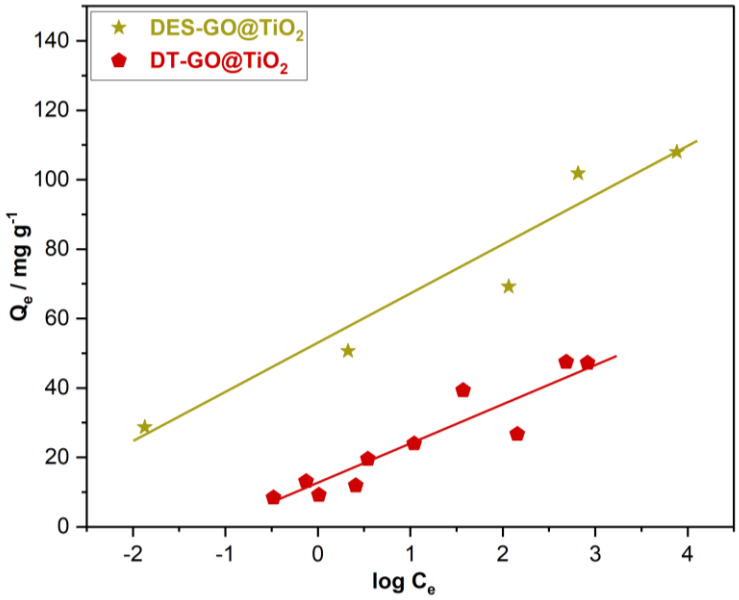

Figure 4.15: Variation of Q_e vs. log C_e and fitted Temkin isotherm model for DT-GO@TiO_2, and DES-GO@TiO_2 at 30°C.

4.3.10 Investigation of MB adsorption with comparable composite material

Table 4.3 compiles data of MB adsorption/removal for DES/surfactant modified NCs [56–60]. When comparing the two modified NCs for rapid removal, DES-GO@TiO_2 has demonstrated superior performance over DT-GO@TiO_2. An examination of the comparative data reveals that DES-GO@TiO_2 exhibits excellent adsorption efficiency, achieving 100% removal within a short time (3 m). This ultrafast removal has been found even better from the recently reported data in the current literature [61]. The adsorption data has been used to compute

the rate of 100% removal of MB per gram of adsorbent per unit time (R=µg of MB per gram of NC per second). This rate data (R) has also been compiled in **Table 4.3**. A perusal of the overall data of **Table 4.3** allows us to state that DES modified adsorbents are distinctly superior to surfactant modified material.

Table 4.3: Comparison of removal efficiency of DES-GO@TiO_2 and DT-GO@TiO_2 with similar materials reported in the literature.

Name of NCs	Adsorbent dosage (g/L)	Initial [MB] (g/L)	Adsorption time (*s*)	Removal efficiency (%)	Rate of MB removal (µg/g of NC/*s*)	References
DES-GO@TiO_2	0.5	0.02	180	~100 %	222	**This Work**
DT-GO@TiO_2	0.5	0.02	900	~100 %	44	
DES-GO@ZrO_2	2	0.02	300	~100 %	33	[60]
CGS-GO@ZrO_2	10	0.04	1200	~100 %	1.1	
DES/GO-Fe_3O_4	0.3	0.025	300	~100 %	277	[61]
PVA/HNT	3	0.04	2400	~100 %	5.5	[62]

4.3.11 Recyclability and reusability Study

The assessment of an adsorbent is based on both its efficiency in adsorption/removal as well as its reusability, which is an important consideration in ensuring the process remains economically viable across several cycles [63–65]. In this investigation, MB adsorbed on both types of NCs has been recycled through washing with different solvents, including water, methanol, ethanol, 0.1M HCl, and 0.1M NaOH. The desorption capability of the adsorbed MB is illustrated in **Figure 4.17**, highlighting ethanol as the most effective solvent for desorbing MB from DES-GO@TiO2 (R_e~90%) and DT-GO@TiO_2 (R_e~86%). **Figure 4.16** illustrates the adsorption-desorption efficiency of MB adsorbed on the NCs. Using ethanol as the recharging solvent, it is effective to recycle and reuse the NCs for up to seven consecutive cycles. The effectiveness of recycling indicates that the MB adsorption process involves physical interaction. The sustained adsorption capacity even after seven cycles indicates that these NCs have the potential to serve as efficient adsorbents for MB or its derivatives [66].

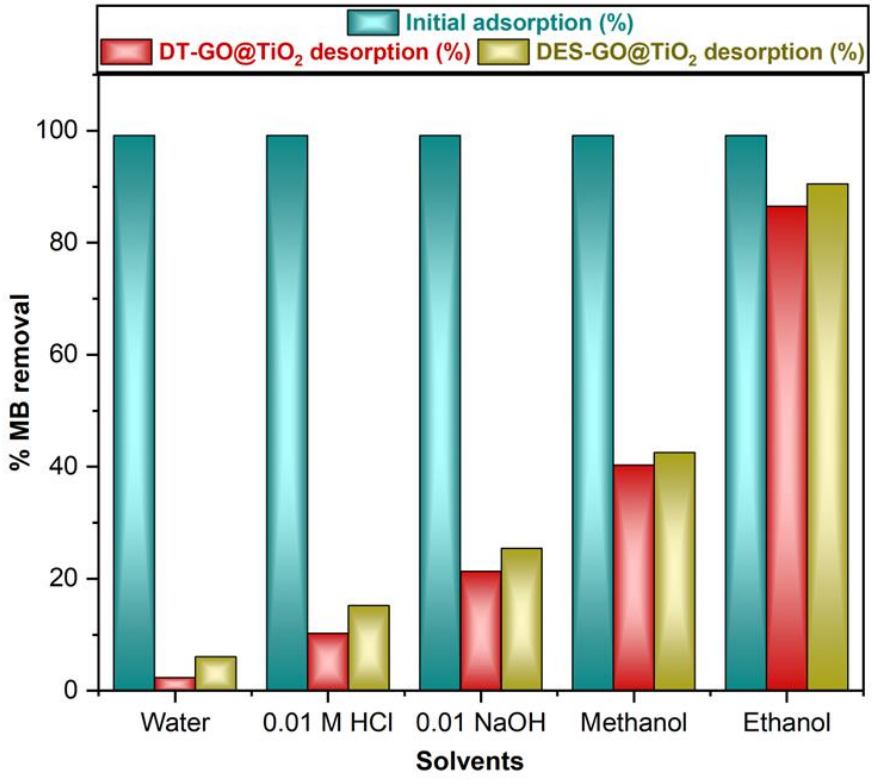

Figure 4.16: Desorption study of MB from DT-GO@TiO_2, and DES-GO@TiO_2 NCs using 50 ml of various solvents.

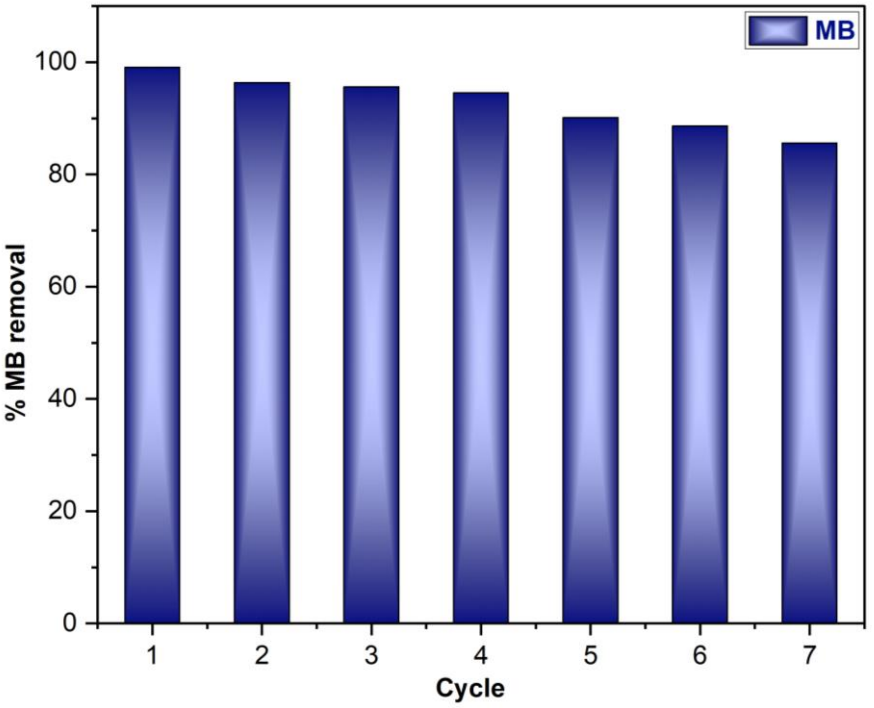

Figure 4.17: Recyclability study of NCs using 50 ml of ethanol for each cycle (up to 7 cycles).

4.3.12 MB adsorption mechanism

The adsorption mechanism of MB on the NCs can be elucidated through various potential interactions [60]. Four primary types of interactions, including electrostatic, hydrogen bonding, Yoshida hydrogen bonding, and n-π interaction, may occur between MB and the NCs, as illustrated in **Scheme 4.1**. Initial FESEM data (**Figure 4.3**) indicate that TiO_2 nanoparticles are evenly distributed on the surface of GO sheets. The dominant factor in the adsorption process appears to be electrostatic attraction, which is notably influenced by the pH of the reaction. MB adsorption was more favourable at higher pH values, particularly at pH 10. At the given reaction pH, the MB dye molecules carried a positive charge, whereas the NCs' surface bore a negative charge. Positively charged MB molecules were able to bind quickly because of the abundance of negatively charged oxygen groups. Furthermore, the MB molecules and NCs' hydrogen bonding facilitated and enhanced the cationic dye's adsorption process. Therefore, increasing the MB solutions' pH resulted in an increase in the electrostatic attraction between the negatively charged surface of both modified NCs and the positively charged MB molecules. Furthermore, the nature of the NCs shifted toward hydrophobicity (attributed to the presence of hydrocarbon chains from DTAB or DES), which further facilitated the attraction of MB molecules to the adsorbent surface.

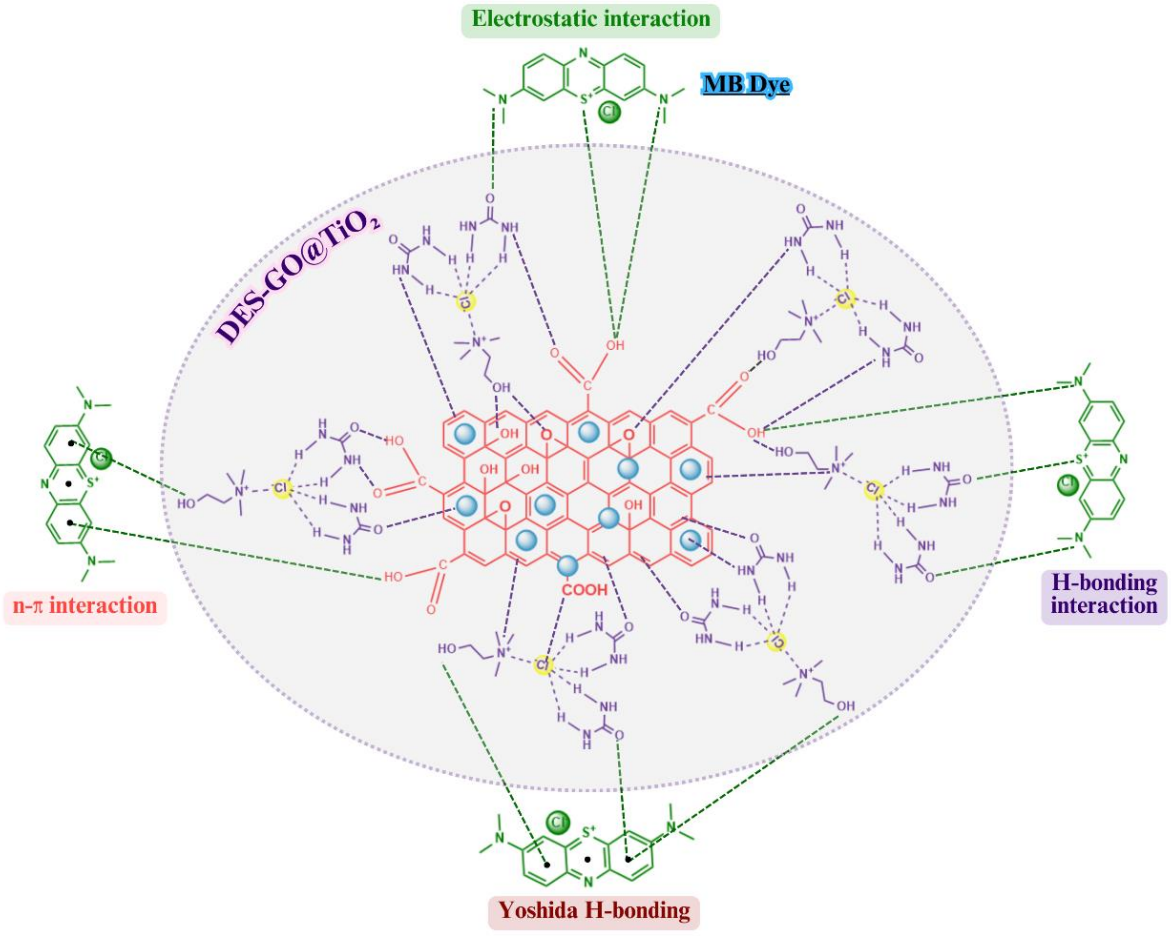

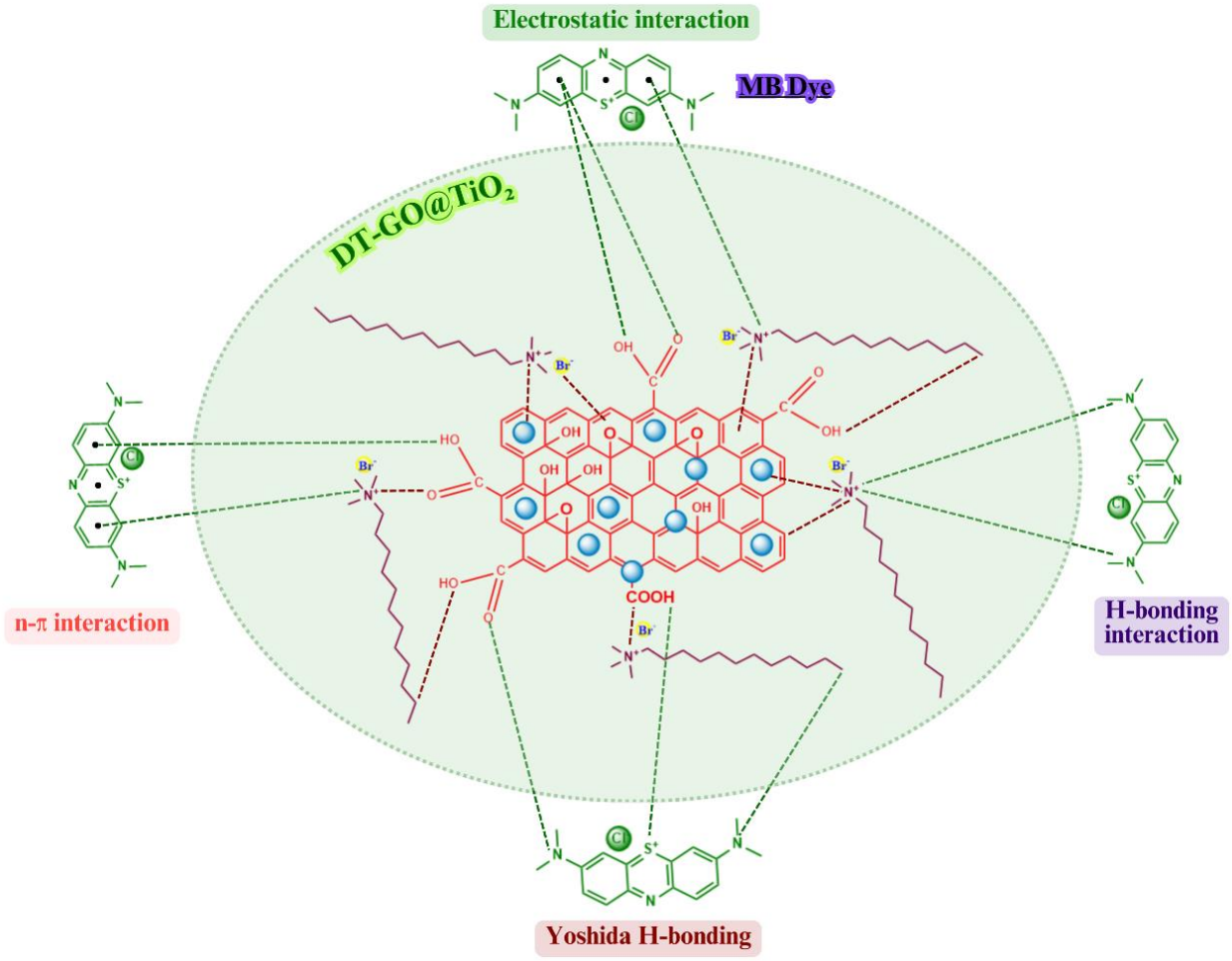

Scheme 4.1: Schematic representation of MB adsorption on DES-GO@TiO_2 and DT-GO@TiO_2 NCs via different modes of interactions.

4.4 Conclusion

In conclusion of this chapter, the work relates the synergy of modifier (DES or DTAB) and NC (GO@TiO_2) to improve the adsorption of a hazardous dye (MB) from aqueous bodies. The material and process have been characterized physiochemically and optimized with respect to adsorbent dose, initial MB content, pH, and contact time, respectively. The adsorption process adheres *pseudo*-second order kinetics and Langmuir adsorption isotherm. The efficiency of the adsorbent follows the order: DES-GO@TiO_2 > DT-GO@TiO_2 > GO@TiO_2. The rate of MB adsorption with DES-GO@TiO_2 has been found 222 µg per gram of adsorbent in one second which shows ultrafast adsorption with this advanced novel material. The perusal of data compiled in **Table 4.3** dictates that DES could be a preferred choice over other classes of material. The sustainability and economy of the process have also been established by repeat adsorption cycles (seven times) without showing any distinct deterioration. The strategy reported here can be used to develop advanced materials (by coupling GO with other metal oxides) for the treatment of industrial effluent where dyes or colouring materials are used. There is a need to perform such

studies to clean the environment/water matrices with material developed based on other natural deep eutectic solvents as they are versatile coupling agents for the members of the graphene family with metal oxide NCs [67–69].

4.5 References

[1] M. T. Yagub, T. K. Sen, S. Afroze, and H. M. Ang, Adv Colloid Interface Sci **209**, 172 (2014).

[2] P. Otero, S. K. Saha, A. Hussein, J. Barron, and P. Murray, Food Anal Methods **10**, 876 (2017).

[3] F. Martin, J.-M. Oberson, M. Meschiari, and C. Munari, Food Chem **197**, 1249 (2016).

[4] T. Rejczak and T. Tuzimski, Food Anal Methods **10**, 3572 (2017).

[5] N. Sharma, S. Tiwari, and R. Saxena, in *Quality Control in the Beverage Industry* (Elsevier, 2019), pp. 123–159.

[6] E. Ayranci and O. Duman, Sep Sci Technol **44**, 3735 (2009).

[7] N. Nasseh, F. S. Arghavan, N. Daglioglu, and A. Asadi, Environmental Science and Pollution Research **28**, 19222 (2021).

[8] N. El-Shafai, M. E. El-Khouly, M. El-Kemary, M. Ramadan, I. Eldesoukey, and M. Masoud, RSC Adv **9**, 3704 (2019).

[9] K. Thangavelu, C. Aubry, and L. Zou, Ind Eng Chem Res **60**, 1266 (2021).

[10] M. Ni, M. K. H. Leung, D. Y. C. Leung, and K. Sumathy, Renewable and Sustainable Energy Reviews **11**, 401 (2007).

[11] H. Zhang, X. Quan, S. Chen, H. Yu, and N. Ma, Chemistry of Materials **21**, 3090 (2009).

[12] Y. Zhu, S. Murali, W. Cai, X. Li, J. W. Suk, J. R. Potts, and R. S. Ruoff, Advanced Materials **22**, 3906 (2010).

[13] C. Su and K. P. Loh, Acc Chem Res **46**, 2275 (2013).

[14] E. D. H. Kong, J. H. F. Chau, C. W. Lai, C. S. Khe, G. Sharma, A. Kumar, S. Siengchin, and M. R. Sanjay, Nanomaterials **12**, 3536 (2022).

[15] H. W. Ha, A. Choudhury, T. Kamal, D.-H. Kim, and S.-Y. Park, ACS Appl Mater Interfaces **4**, 4623 (2012).

[16] Y. Qi, M. Yang, W. Xu, S. He, and Y. Men, J Colloid Interface Sci **486**, 84 (2017).

[17] Y. Kuang, R. Yang, Z. Zhang, J. Fang, M. Xing, and D. Wu, Chemosphere **236**, 124416 (2019).

[18] Z. Wu, H. Zhong, X. Yuan, H. Wang, L. Wang, X. Chen, G. Zeng, and Y. Wu, Water Res **67**, 330 (2014).

[19] S. Singh, B. Patel, K. Parikh, and S. Kumar, ChemistrySelect **5**, 14230 (2020).

[20] C. Gan, T. Liang, W. Li, X. Fan, and M. Zhu, Appl Surf Sci **491**, 105 (2019).

[21] V. Agarwal, Y. Fadil, A. Wan, N. Maslekar, B. N. Tran, R. A. Mat Noor, S. Bhattacharyya, J. Biazik, S. Lim, and P. B. Zetterlund, ACS Appl Mater Interfaces **13**, 18338 (2021).

[22] M. Yusuf, M. A. Khan, M. Otero, E. C. Abdullah, M. Hosomi, A. Terada, and S. Riya, J Colloid Interface Sci **493**, 51 (2017).

[23] Y. Wu, H. Luo, H. Wang, C. Wang, J. Zhang, and Z. Zhang, J Colloid Interface Sci **394**, 183 (2013).

[24] B. Patel, S. Singh, K. Parikh, V. Chavda, D. Hirpara, D. Ray, V. K. Aswal, and S. Kumar, J Mol Liq **359**, 119242 (2022).

[25] B. Patel, S. Singh, K. Parikh, V. Chavda, D. Ray, V. K. Aswal, and S. Kumar, J Mol Liq **363**, 119885 (2022).

[26] J. Su, S. He, Z. Zhao, X. Liu, and H. Li, Colloids Surf A Physicochem Eng Asp **554**, 227 (2018).

[27] J. Xu, X. Cai, and F. Shen, Appl Surf Sci **379**, 433 (2016).

[28] N. Jain, S. Trabelsi, S. Guillot, D. McLoughlin, D. Langevin, P. Letellier, and M. Turmine, Langmuir **20**, 8496 (2004).

[29] H. Li and C. P. Tripp, Langmuir **18**, 9441 (2002).

[30] S. Chen, W. Wang, and W. Xu, Mater Lett **180**, 196 (2016).

[31] P. A. Shah, P. S. Shrivastav, V. S. Sharma, and V. Chavda, Bioanalysis **15**, 815 (2023).

[32] P. A. Shah, V. Chavda, D. Hirpara, V. S. Sharma, P. S. Shrivastav, and S. Kumar, J Mol Liq **390**, 123171 (2023).

[33] A. Azzouz and M. Hayyan, Chemical Engineering Journal **468**, 143563 (2023).

[34] L. I. N. Tomé, V. Baião, W. da Silva, and C. M. A. Brett, Appl Mater Today **10**, 30 (2018).

[35] S. Datta, C. Jo, M. De Volder, and L. Torrente-Murciano, ACS Appl Mater Interfaces **12**, 18803 (2020).

[36] J. A. Hammons and J. Ilavsky, Electrochim Acta **228**, 462 (2017).

[37] M. Atilhan, L. T. Costa, and S. Aparicio, Langmuir **33**, 5154 (2017).

[38] M. Hayyan, A. Abo-Hamad, M. A. AlSaadi, and M. A. Hashim, Nanoscale Res Lett **10**, 324 (2015).

[39] Y. Huang, Y. Wang, Q. Pan, Y. Wang, X. Ding, K. Xu, N. Li, and Q. Wen, Anal Chim Acta **877**, 90 (2015).

[40] X.-Z. Tang, Z. Cao, H.-B. Zhang, J. Liu, and Z.-Z. Yu, Chemical Communications **47**, 3084 (2011).

[41] R. A. K. Rao, S. Singh, B. R. Singh, W. Khan, and A. H. Naqvi, J Environ Chem Eng **2**, 199 (2014).

[42] R. Wang, K. Shi, D. Huang, J. Zhang, and S. An, Sci Rep **9**, 18744 (2019).

[43] H. Zhang, X. Wang, N. Li, J. Xia, Q. Meng, J. Ding, and J. Lu, RSC Adv **8**, 34241 (2018).

[44] R. Wang, K. Shi, D. Huang, J. Zhang, and S. An, Sci Rep **9**, 18744 (2019).

[45] C. C. Caliman, A. F. Mesquita, D. F. Cipriano, J. C. C. Freitas, A. A. C. Cotta, W. A. A. Macedo, and A. O. Porto, RSC Adv **8**, 6136 (2018).

[46] J. Shen, B. Yan, M. Shi, H. Ma, N. Li, and M. Ye, J Mater Chem **21**, 3415 (2011).

[47] A. Bansal, A. Kumar, P. Kumar, S. Bojja, A. K. Chatterjee, S. S. Ray, and S. L. Jain, RSC Adv **5**, 21189 (2015).

[48] J. T. Adeleke, T. Theivasanthi, M. Thiruppathi, M. Swaminathan, T. Akomolafe, and A. B. Alabi, Appl Surf Sci **455**, 195 (2018).

[49] N. Nasseh, F. S. Arghavan, N. Daglioglu, and A. Asadi, Environmental Science and Pollution Research **28**, 19222 (2021).

[50] Z. Jiaqi, D. Yimin, L. Danyang, W. Shengyun, Z. Liling, and Z. Yi, Colloids Surf A Physicochem Eng Asp **572**, 58 (2019).

[51] H. Yuh-Shan, Scientometrics **59**, 171 (2004).

[52] A. E. Ofomaja, E. B. Naidoo, and S. J. Modise, Desalination **251**, 112 (2010).

[53] V. Selen, Ö. Güler, D. Özer, and E. Evin, Desalination Water Treat **57**, 8826 (2016).

[54] Y. Liu, Colloids Surf A Physicochem Eng Asp **274**, 34 (2006).

[55] M. Saxena, N. Sharma, and R. Saxena, Surfaces and Interfaces **21**, 100639 (2020).

[56] L. Cui, X. Guo, Q. Wei, Y. Wang, L. Gao, L. Yan, T. Yan, and B. Du, J Colloid Interface Sci **439**, 112 (2015).

[57] H. Shi, W. Li, L. Zhong, and C. Xu, Ind Eng Chem Res **53**, 1108 (2014).

[58] H. V Tran, L. T. Bui, T. T. Dinh, D. H. Le, C. D. Huynh, and A. X. Trinh, Mater Res Express **4**, 035701 (2017).

[59] S. Yang, T. Zeng, Y. Li, J. Liu, Q. Chen, J. Zhou, Y. Ye, and B. Tang, J Nanomater **2015**, 1 (2015).

[60] V. Chavda, B. Patel, S. Singh, D. Hirpara, V. D. Rajeswari, and S. Kumar, RSC Sustainability (2023).

[61] N. Mehrabi, U. F. Abdul Haq, M. T. Reza, and N. Aich, J Environ Chem Eng **8**, 104222 (2020).

[62] A. P. Nambiar, R. Pillai, Y. Vadikkeettil, M. Sanyal, and P. S. Shrivastav, Mater Chem Phys **291**, 126752 (2022).

[63] C. Liu, A. M. Omer, and X. Ouyang, Int J Biol Macromol **106**, 823 (2018).

[64] G. R. Mahdavinia, M. Soleymani, M. Sabzi, H. Azimi, and Z. Atlasi, J Environ Chem Eng **5**, 2617 (2017).

[65] L. M. Sanchez, R. P. Ollier, and V. A. Alvarez, Journal of Polymer Research **26**, 142 (2019).

[66] M. Wainwright, Int J Antimicrob Agents **16**, 381 (2000).

[67] M. Marchel, M. P. Rayaroth, C. Wang, L. Kong, J. A. Khan, and G. Boczkaj, Chemical Engineering Journal **475**, 144971 (2023).

[68] Z. Lin, X. Liu, and B. Jiao, TrAC Trends in Analytical Chemistry **159**, 116923 (2023).

[69] Q. Zaib, Z. Masoumi, N. Aich, and D. Kyung, J Environ Chem Eng **11**, 110214 (2023).